International Journal of Multiphysics
Volume 18, No. 4, 2024
ISSN: 1750-9548

Er^{+}-Doped Magnesium Ferrite Nanoparticles' Structural, Optical, And Thermal Characteristics Produced Using the Sol-Gel Combustion Technique

Jeedi Adam[1,2*], Katrapally Vijaya Kumar[1]
[1]Department of Physics, JNTUH University College of Engineering Sultanpur, Pulkal (M), Sanga Reddy (D), 502273, Telangana, India
[2]Department of Physics, Government Polytechnic, Warangal, 506002, Telangana, India

* Corresponding Author.
email id: adamjeedi@gmail.com (Jeedi Adam)

Abstract

$MgEr_xFe_{2-x}O_4$ (x = 0.00, 0.05, 0.10) ferrites samples crystallize in a single-phase cubic spinel structure (Fd-3m), according to Rietveld-refined XRD patterns. Successful Er integration is demonstrated by the excellent match between calculated and observed profiles as well as the lack of subsequent phases. Lattice distortion caused by Er replacement without symmetry modification is reflected in small peak shifts. $MgEr_xFe_{2-x}O_4$ nanoparticles' UV-Vis absorption spectra show a wide absorption band in the 600 - 650 nm range, which is typical of spinel ferrites. Because of lattice distortion and variations in cation distribution, Er substitution alters the absorption intensity. Reduced absorbance from longer annealing times suggests better crystallinity and fewer states linked to defects. These findings show that the optical characteristics of $MgEr_xFe_{2-x}O_4$ ferrites are efficiently tuned by both Er doping and thermal treatment. All things considered, Er doping and annealing work together to effectively tune the optical band gap of $MgEr_xFe_{2-x}O_4$ ferrites, making these materials attractive options for photocatalytic, sensor, and visible-light-driven optoelectronic applications. The DSC curves of $MgEr_xFe_{2-x}O_4$ exhibit a broad endothermic zone with no abrupt transitions up to 400 °C, showing strong thermal stability of the spinel phase, and an endothermic peak below ~100 °C due to moisture elimination. The heat-flow behavior is slightly altered by Er substitution, indicating better lattice stabilization without phase transformation. Progressive crystallization and lattice relaxation are indicated by expanded DSC curves, which display a slow increase in heat-flow without noticeable crystallization peaks. The crystallization slope is somewhat altered by Er substitution, indicating improved thermal stabilization and defect-controlled grain development devoid of phase change. With the maximum melting and crystallization temperatures at x = 0.05, the TG-DTA curves demonstrate a significant dopant-dependent shift in thermal transitions, suggesting improved thermal stability. In line with previous results on doped ferrites, the variations in heat-flow intensity reflect dopant-induced lattice deformation and changed cation-oxygen bonding.

Keywords: Mg-Erferrite: optical, thermal, and structural characteristics.

1. Introduction

Because of their exceptional magnetic, electrical, optical, and thermal properties, spinel ferrites with the general chemical formula $MgFe_2O_4$ (M = Mg, Ni, Zn, Co, etc.) make up a significant class of functional oxide materials that can be used in magnetic recording, sensors, microwave devices, energy storage, photocatalysis, and biomedical fields [1,2]. Among these, magnesium ferrite ($MgFe_2O_4$) is a soft magnetic n-type semiconductor that crystallizes in the cubic spinel structure (Fd-3m space group). It has excellent chemical and thermal stability, low eddy current losses, mild saturation magnetization, and high electrical resistivity [1,3].

Controlled cation substitution may efficiently adjust the physical properties of $MgFe_2O_4$, which are particularly sensitive to lattice distortions and cation distribution [3-5]. Due to the high ionic radii, strong spin-orbit coupling, and localized 4f electronic states of rare-earth ions, rare-earth (RE^{3+}) ion doping has become a potent method in recent years to alter the structural and functional behavior of spinel ferrites [4,6]. Significant

changes in lattice parameters, micro-strain, cation occupancy between tetrahedral (A) and octahedral (B) sites, and super-exchange interactions result from the substitution of RE^{3+} ions at Fe^{3+} sites [5-8].

Erbium (Er^{3+}), one of the rare-earth dopants, has garnered particular interest because of its complicated 4f electronic structure, significant magnetocrystalline anisotropy, and relatively large magnetic moment [6,9]. The ionic size disparity between Er^{3+} and Fe^{3+} causes lattice distortion when Er^{3+} ions are incorporated into the $MgFe_2O_4$ lattice, leading to strain-mediated effects and defect production [4,7]. By strengthening B-B contacts and weakening A-B superexchange interactions, these structural changes adjust magnetic properties like coercivity and saturation magnetisation [5,9]. Furthermore, band-gap engineering and improved visible-light absorption are made possible by Er doping, which creates localized electronic states within the band structure. These properties are advantageous for optoelectronic and photocatalytic applications [7,8,10].

Rare-earth-doped magnesium ferrites are appropriate for high-temperature magnetic and electrical applications because of their enhanced phase stability and inhibited grain development as a result of rare-earth-induced grain boundary pinning [6,10]. Er-substituted $MgFe_2O_4$ ferrites are therefore a promising multifunctional material system in which dopant concentration and synthesis circumstances can efficiently design structural, magnetic, optical, and thermal properties. With a focus on their potential for sophisticated magnetic and optoelectronic applications, the current study focuses on the synthesis and methodical investigation of Er-doped $MgFe_2O_4$ferrites with the goal of establishing distinct correlations between erbium substitution, structural evolution, and functional properties. The current study is motivated by the fact that, despite these benefits, there is still a lack of systematic knowledge regarding how Er^{3+} substitution concurrently affects the crystal structure, cation distribution, thermal stability, and opto-magnetic properties of $MgFe_2O_4$ ferrites, especially at low-doping-concentrations.

2. Experimental

Citric acid was used as the fuel source, and the starting chemicals were magnesium nitrate hexahydrate ($Mg(NO_3)_2$ $6H_2O$, 99%, Sigma Aldrich), iron(III) nitrate nonahydrate ($Fe(NO_3)_3$ $9H_2O$, 98-100%, A.R, grade Merck), and erbium(III) nitrate pentahydrate ($Er(NO_3)_3$ $5H_2O$, 99.9%, Sigma Aldrich). The initial materials used were analytical grade and did not undergo additional purification processes. Using the auto-combustion approach, a precursor consisting of a mixture of $Mg(NO_3)_2$ $6H_2O$, $Fe(NO_3)_3$ $9H_2O$, $Er(NO_3)_3$ $5H_2O$, and citric acid was made in an aqueous solution. A homogenous solution was achieved by vigorously mixing the nitrates with deionised water. To guarantee a homogenous mixture of metal nitrates, three molar ratios of citric acid were added as a gel agent to the precursors and then agitated for four hours using a magnetic stirrer. To keep the pH level in this solution at 7, NH_3 was added. On a magnetic hot plate, the finished mixture was continually stirred and gradually heated to 100 °C. Producing a viscous gel was the end result [11,12]. When the gel reached 200 °C, an eruption occurred. A loose powder residue was left behind after the dry gel underwent self-sustaining complete combustion. After that, a mortar and pestle were used to carefully ground the product into a fine powder.

The structural, morphological, optical, and magnetic properties of $MgEr_xFe_{2-x}O_4$ (x=0.00, 0.05, and 0.10) nano-ferrites were thoroughly examined. For XRD analysis, a Rigaku Ultima IV diffractometer (Rigaku, Japan) with a 2θ range of 20° to 80° was utilized. The UV-Vis analysis was carried out using an Agilent Technologies Carry 5000-UV-Vis-NIR spectrophotometer.

3. Results and discussions

3.1. Rietveld refinement

Fig. 1, shows the Rietveld-refined X-ray diffraction patterns of $MgEr_xFe_{2-x}O_4$ (x = 0.00, 0.05, and 0.10) nanoparticles are displayed in Fig. 1 (a–c). The computed patterns

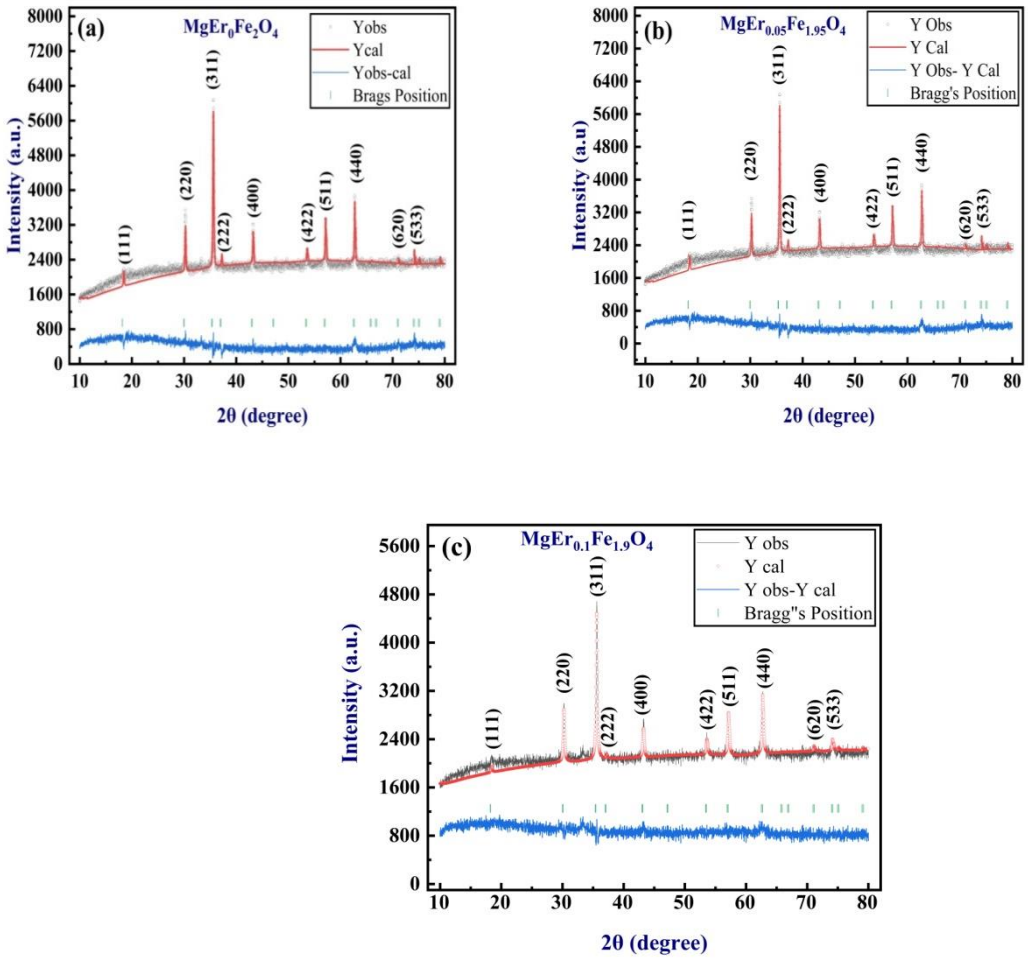

Fig 1. Rietveld refinement plots of $MgEr_xFe_{2-x}O_4$ (a) x=0.00 (b) x=0.05 and (c) x=0.10 samples.

X	D (nm)	a (Å)	E_g (eV)	Crystallization Temperature ˚C	Heat flow mW	Melting Temperature ˚C	Heat flow mW
0.00	39.423	7.9701	1.859	205.35	4.7988	205.99	4.7641
0.05	38.205	8.5811	1.853	395.23	7.5153	396.43	7.4826
0.10	30.6466	7.9725	1.823	296.33	5.3934	297.00	5.3209

Table 1: Grain size D (nm), Lattice constant a (Å), Band gap energy E_g in eV, Crystallization Temperature ˚C, Heat flow mW, Melting Temperature ˚C and Heat flow mW.

(Y_cal) and the measured diffraction profiles (Y_obs) correspond quite well, and the difference curves (Y_obs - Y_cal) show little residual intensity, indicating that the refinement was of outstanding quality. The cubic spinel phase's Bragg reflection locations are indicated by the vertical tick marks [13,14].The occurrence of distinctive reflections indexed to the x (111), (220), (311), (222), (400), (422), (511), (440), (620), and (533) planes indicates that all compositions crystallize in a single-phase cubic spinel structure with space group Fd-3m. The efficient

integration of Er^{3+} ions into the spinel lattice within the examined composition range is confirmed by the lack of any additional peaks associated with secondary phases like ErO_2 or iron oxides.

For all samples, the diffraction pattern is dominated by the strongest (311) reflection, suggesting a preferential spinel crystallographic orientation characteristic of ferrites based on magnesium. The substitution of bigger Er^{3+} ions (ionic radius ≈ 1.06Å) for Fe^{3+}ions (≈ 0.645Å) results in lattice distortion, which is responsible for the minor peak intensity alteration and subtle peak-position shifts that are seen, as the Er concentration increases. Without changing the overall spinel symmetry, such substitution results in modifications to the lattice parameter, the distribution of cations between tetrahedral (A) and octahedral (B) sites, and local strain [15, 16].

Good crystallinity and homogenous phase development are further shown by the well-fitted peak forms and smooth background profile. Er doping introduces regulated structural deformation rather than disrupting the core spinel framework, as confirmed by the low mismatch between calculated and experimental patterns. These findings are in line with documented Rietveld refinement investigations on rare-earth-doped ferrites, in which strain accommodation and lattice expansion take place without phase segregation. All things considered, the Rietveld refinement unequivocally shows that $MgEr_xFe_{2-x}O_4$ ferrites maintain a thermally and structurally stable cubic spinel phase with Er substitution, indicating their potential for high-temperature functional, advanced magnetic, and optical applications.

According to Table 1, the crystallite size (D), as determined by the Scherrer formula, systematically falls with dopant concentration, going from 39.42 nm (x = 0) to 38.21 nm (x = 0.05) and then to 30.65 nm at x = 0.10. By causing lattice strain and impeding crystallite coalescence, dopant inclusion limits grain development, as evidenced by this drop. According to Table 1, the lattice constant (a) varies slightly with composition, rising from 7.9701 Å for x = 0 to 8.5811 Å for x = 0.05 before falling to 7.9726 Å at x = 0.10. This suggests that there is some structural distortion and lattice relaxation at higher doping levels.

3.2. UV-Vis. spectroscopy

The visible region (≈550-750 nm) UV - Vis absorption spectra of $MgEr_xFe_{2-x}O_4$ ferrite nanoparticles for varying annealing durations are displayed in Fig. 2 (a-c). As is typical of spinel ferrites, all compositions show a broad absorption band centered in the orange - red spectral region (~600 - 650 nm). This band is typically attributed to crystal-field d - d transitions of Fe^{3+} ions at tetrahedral (A) and octahedral (B) sites, as well as $O^{2-} \rightarrow Fe^{3+}$ charge-transfer transitions.

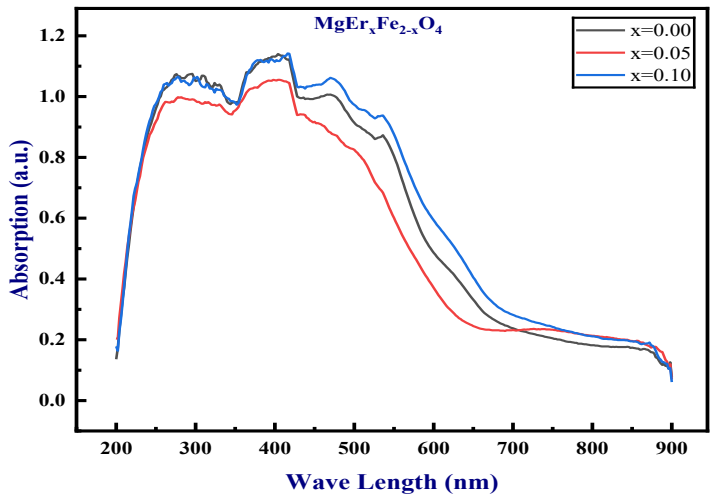

Fig. 2. UV curves of $MgEr_xFe_{2-x}O_4$ (x = 0.00, 0.05 and 0.10) ferrites.

$MgEr_xFe_{2-x}O_4$(x = 0.00, 0.05, and 0.10) exhibits significant absorption in the UV and visible regions, followed by a steady decrease towards the near-infrared region, according to the UV–Vis absorption spectra obtained in the 200–900 nm range as shown in Fig. 2. $O^{2-} \rightarrow Fe^{3+}$ charge-transfer transitions at the tetrahedral (A) and octahedral (B) sites of the spinel lattice are primarily responsible for the broad absorption band seen in all samples, which spans from approximately 250 to 550 nm and is typical of spinel ferrites. Defect-related localised states within the band gap and crystal-field d–d transitions of Fe^{3+} ions are responsible for the faint absorption tail seen beyond about 600 nm.

Absorption intensity and edge position show a discernible change with increasing Er substitution. In comparison to the undoped ferrite, the absorption edge of Er-doped samples exhibits a little red shift towards longer wavelengths, suggesting a modest narrowing of the optical band gap. Lattice distortion caused by the greater ionic radius of Er ions replacing Fe at octahedral sites, which alters the Fe–O bond length and increases structural disorder, can be linked to this behaviour. Additionally, the inclusion of Er creates more localised energy states close to the conduction band, which makes electronic transitions at lower photon energies easier. Defect-mediated transitions and sp–d exchange interactions between localised f-electrons of rare-earth ions and the band electrons of the host lattice are linked to similar red-shift behaviour and absorption enhancement in rare-earth-doped ferrites, which have been extensively documented [17 – 19]. We observed that $MgEr_xFe_{2-x}O_4$ ferrites appear to be interesting candidates for optoelectronic, photocatalytic, and UV-shielding applications due to the significant absorption in the visible range and the tunability of the absorption edge with Er content.

3.3. Photocatalytic analysis

Fig. 3 shows the photocatalytic properties of $MgEr_xFe_{2-x}O_4$(x=0.00, 0.05, 0.10) ferrite samples. A comparatively higher absorbance intensity is seen for the undoped $MgFe_2O_4$ sample (Fig. 3 (a)), suggesting enhanced optical density brought on by a higher concentration of Fe^{3+} ions involved in electronic transitions. Absorption intensity and spectral shape gradually change when Er^{3+} substitution increases (x = 0.05 and 0.10) (Fig.3(b) and (c)). This behavior can be explained by the partial substitution of Er^{3+} ions for Fe^{3+}ions, which modifies the cation distribution between A and B sites, the local crystal field environment, and the lengths of Fe-O bonds. Because Er^{3+} has a greater ionic radius, it causes defect states and lattice distortion, which affects the likelihood of electronic transitions.

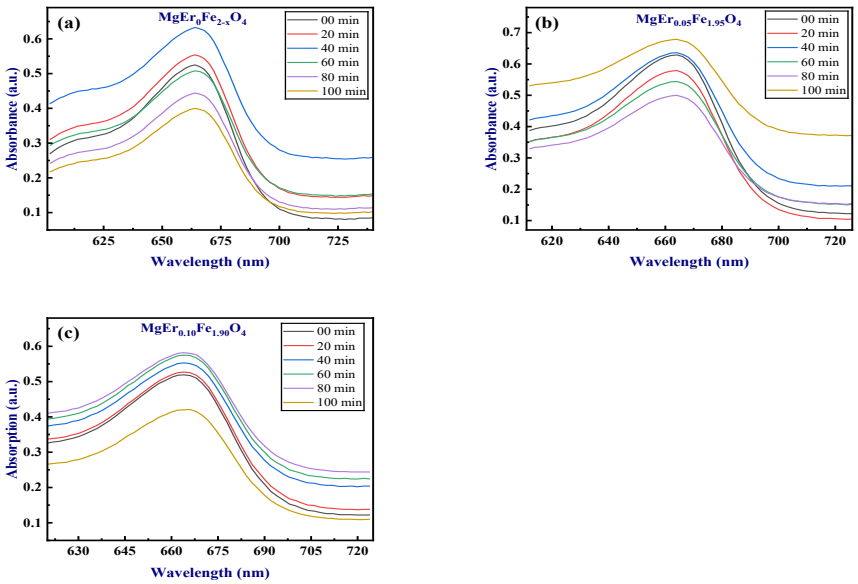

Fig. 3. Photocatalytic absorbance-wavelength curves of $MgEr_xFe_{2-x}O_4$ (x = 0.00, 0.05 and 0.10) ferrites.

All compositions show a discernible impact of annealing time. Improved crystallinity, grain development, and decreased defect density are the reasons why samples that have been annealed for longer periods of time exhibit lower absorbance intensity and a smoother absorption edge. Lower sub-band-gap absorption results from the reduction of localized states inside the band gap caused by the decrease in structural disorder. By preserving a greater density of flaws and grain boundaries, shorter annealing durations, on the other hand, improve light absorption through localized states.

The optical response of $MgEr_xFe_{2-x}O_4$ ferrites is greatly influenced by the combined effects of Er doping and annealing duration. These materials may be suitable for opto-magnetic devices, visible-light absorbers, photocatalytic or sensor-related applications where defect-assisted absorption and band-gap tuning are desired, as indicated by the controlled modulation of absorption in the visible region.

3.4. Tauc plots

The Tauc plots of $MgEr_xFe_{2-x}O_4$(x = 0.00, 0.05, and 0.10) nanoparticles are shown in 4 (a-c), showing a direct permitted electronic transition consistent with previous results on spinel ferrites [17, 18]. The linear portion of the plots was extrapolated to $\alpha h\nu\gamma=A(h\nu - E_g)$ in order to determine the optical band gap values. The semiconducting nature of magnesium-based ferrites is confirmed by the obtained E_g values, which are displayed in Table 1 and lie within the-visible-region.

Er^{3+} substitution results in a consistent change in E_g. Lattice distortion, cation redistribution, and the formation of defect-related localized states close to the conduction and valence band boundaries are responsible for the small decrease in the band gap for Er-doped samples [19, 20]. By altering Fe - bond lengths and inducing structural strain, Er^{3+} 's greater ionic radius than Fe^{3+} reduces the effective band gap through defect-assisted electronic transitions and increased orbital overlap.

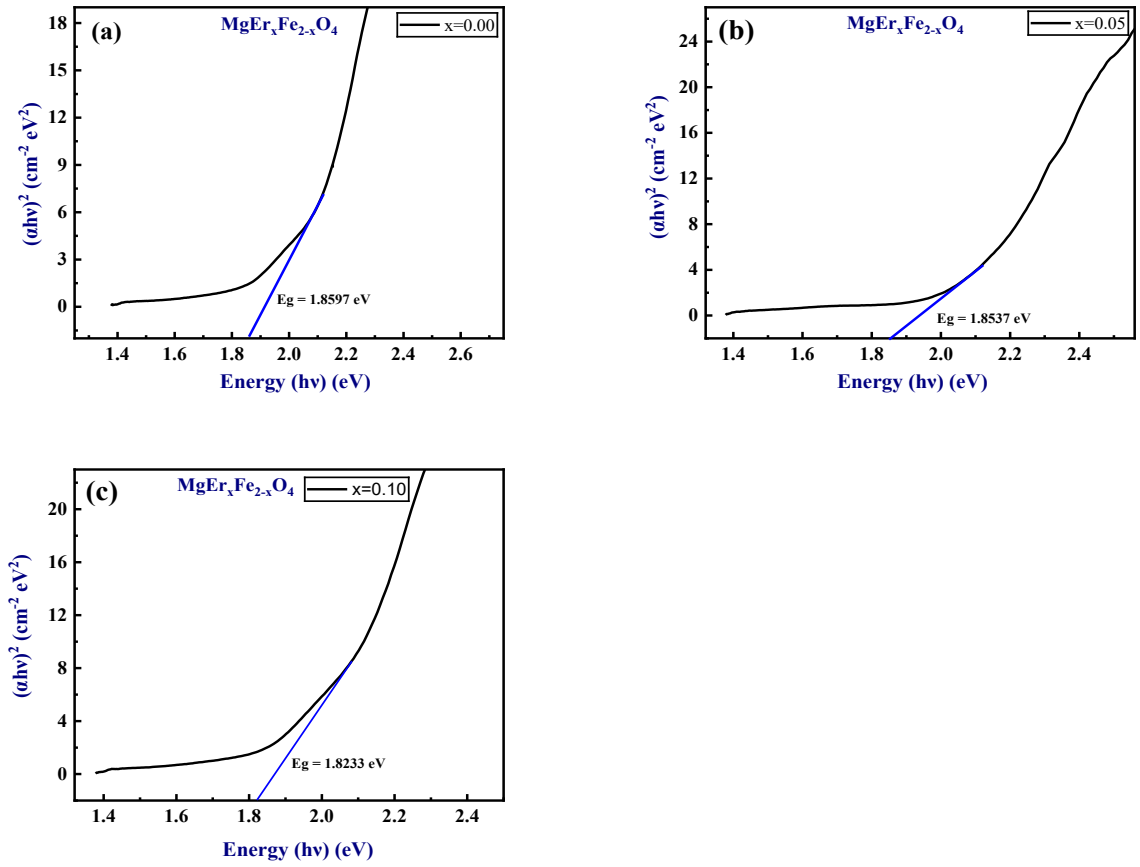

Fig. 4. Tauc plots of $MgEr_xFe_{2-x}O_4$ (x = 0.00, 0.05 and 0.10) ferrites.

With increasing dopant concentration, the optical band-gap energy (E_g), which is calculated from the Tauc plot for direct transitions, gradually decreases. E_g drops from 1.859 eV for the undoped sample (x = 0) to 1.853 eV at x = 0.05 and then to 1.823 eV for x = 0.10, as indicated in Table 1. Dopant-induced lattice disorder, localized defect states, and increased structural strain are usually blamed for this ongoing narrowing of the band gap. These factors work together to encourage band-tailing and lower the energy needed for electron excitation. Increased defect-mediated electronic transitions with higher doping levels are confirmed by the observed red shift in the absorption edge.

Additionally, the evolution of the absorption edge is in line with the impact of annealing or thermal treatment, which enhances crystallinity and lessens microstructural disorder. A more distinct absorption edge and persistent band-gap values result from annealing-induced grain expansion suppressing localized tail states (Urbach energy) [20, 21]. For rare-earth-substituted spinel ferrites and $MgFe_2O_4$-based spinel ferrites produced under various calcination settings, similar patterns have been extensively documented.

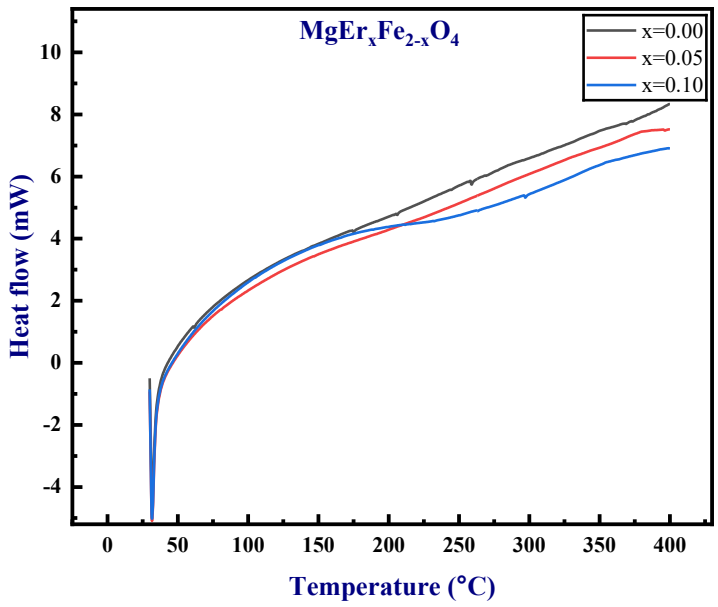

Fig. 5 DSC analysis of $MgEr_xFe_{2-x}O_4$ (x = 0.00, 0.05 and 0.10) ferrites.

3.5. Diffferential scanning calorimetry

$MgEr_xFe_{2-x}O_4$ ferrites are interesting candidates for visible-light-driven optoelectronic, photocatalytic, and sensor applications because of the combined effect of Er doping and annealing, which effectively tunes the optical band gap of these materials [20–23].The DSC thermograms of $MgEr_xFe_{2-x}O_4$(x = 0.00, 0.05, and 0.10) recorded in the temperature range up to about 400 °C are displayed in Fig. 5. Below about 100 °C, all compositions show a noticeable endothermic feature that is explained by the elimination of physically adsorbed moisture and leftover solvents that were trapped in the porous ferrite matrix. This behavior validates the removal of weakly bound species during initial heating and is typical of chemically synthesized spinel ferrites [23, 24].

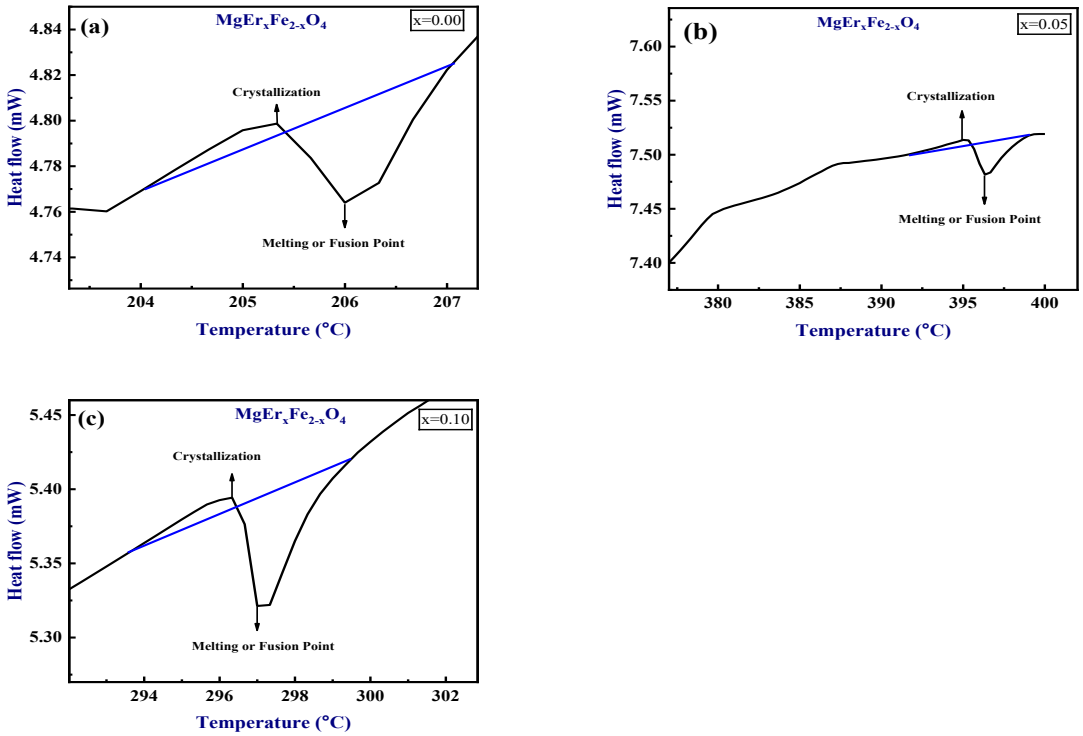

Fig. 6. DSC heat-flow curves of $MgEr_xFe_{2-x}O_4$ (x = 0.00, 0.05 and 0.10) ferrites in the higher temperature region.

A broad and steady endothermic trend without any distinct phase-transition peaks is seen at higher temperatures, suggesting that structural phase change is not present in the temperature range under investigation. The gradual relaxation of lattice strain, the redistribution of cations between tetrahedral (A) and octahedral (B) sites, and the stabilization of the spinel structure are all suggested by the smooth heat-flow change. The cubic spinel phase of $MgEr_xFe_{2-x}O_4$ is thermally stable up to 400 °C, as confirmed by the absence of sudden thermal events.

The minor change in heat-flow amplitude with increasing x clearly indicates the influence of Er^{3+} replacement. Due to increased lattice stiffness and stronger metal - oxygen interaction brought about by the addition of bigger Er^{3+} ions, the Er-doped samples show slightly less heat flow at higher temperatures than the undoped composition. Er inclusion enhances thermal robustness by inhibiting defect-mediated relaxation processes in rare-earth doped ferrites, according to similar patterns. The DSC results show that there is no thermal instability caused by Er substitution, which makes $MgEr_xFe_{2-x}O_4$ ferrites appropriate for high-temperature magnetic and electrical applications.

The extended DSC heat-flow curves of $MgEr_xFe_{2-x}O_4$(x = 0.00, 0.05, and 0.10) in the higher temperature range are shown in Fig.6 (a - c), emphasizing the ferrite nanoparticles' crystallisation and structural relaxation behavior. The fact that none of the compositions show a strong exothermic crystallization peak but rather a continuous endothermic trend suggests that crystallization occurs gradually as opposed to abruptly [24, 25]. Grain growth and nucleation overlap over a wide temperature range in chemically synthesized spinel ferrites, which exhibit this behavior.

The linear increase in heat flow with temperature for the undoped $MgFe_2O_4$sample (Fig. 6 (a)) indicates continuous ordering of Fe^{3+} ions and relaxation of lattice strain, which stabilizes the cubic spinel structure. The lack of a clear crystallization peak indicates that the spinel phase was already established before the DSC measurement, and additional heating mostly increases crystallinity rather than creating a new phase.

The heat-flow slope is marginally altered with Re^{3+} substitution (x = 0.05 and 0.10) (Fig.6 b and c), indicating the impact of rare-earth incorporation on crystallization kinetics. Because Er^{3+} ions have a higher ionic radius than Fe^{3+}, they cause defect-mediated relaxation and local lattice distortion, which expands the crystallization region. In line with rare-earth induced pinning of grain boundaries, the smoother thermal response in Er-doped samples suggests reduced fast grain coalescence and improved thermal stabilization.

The DSC results show that Er doping favors a thermally stable, slowly crystallizing spinel lattice rather than causing the production of any secondary phases. $MgEr_xFe_{2-x}O_4$ ferrites are structurally strong and appropriate for applications requiring thermal endurance and phase stability, such as magnetic devices and high-temperature sensors, as evidenced by the gradual nature of crystallization and the lack of abrupt thermal events.

As seen in Fig.6, the DSC thermograms clearly illustrate that the dopant concentration affects both the melting and crystallisation temperatures. The crystallisation and melting temperatures for the undoped sample (x = 0.00) are 205.35 °C and 205.99 °C, respectively, with corresponding heat-flow values of about 4.8 mW. A notable change is seen at x = 0.05, when the melting temperature rises to 396.43 °C and the crystallization temperature rises dramatically to 395.23 °C. Higher heat-flow signals (~7.5 mW) are also detected, suggesting improved thermal stability and greater endothermic/exothermic responses. Both temperatures drop to 297 °C (melting) and 296.33 °C (crystallisation) at x = 0.10, with modest heat-flow values (~5.3 mW), indicating diminished thermal stability and partial structural relaxation in comparison to the x = 0.05 composition. The thermal transitions are generally highly modulated by the dopant concentration, which reflects the compositional influence on phase stability and energy absorption properties.

3.6. TG-DTA analysis

The combined TG-DTA thermograms in Fig.7 demonstrate a clear relationship between thermal behavior and dopant concentration. The undoped sample (x = 0.00) shows a single significant weightloss event between ~50 - 250 °C, along with a small exothermic peak

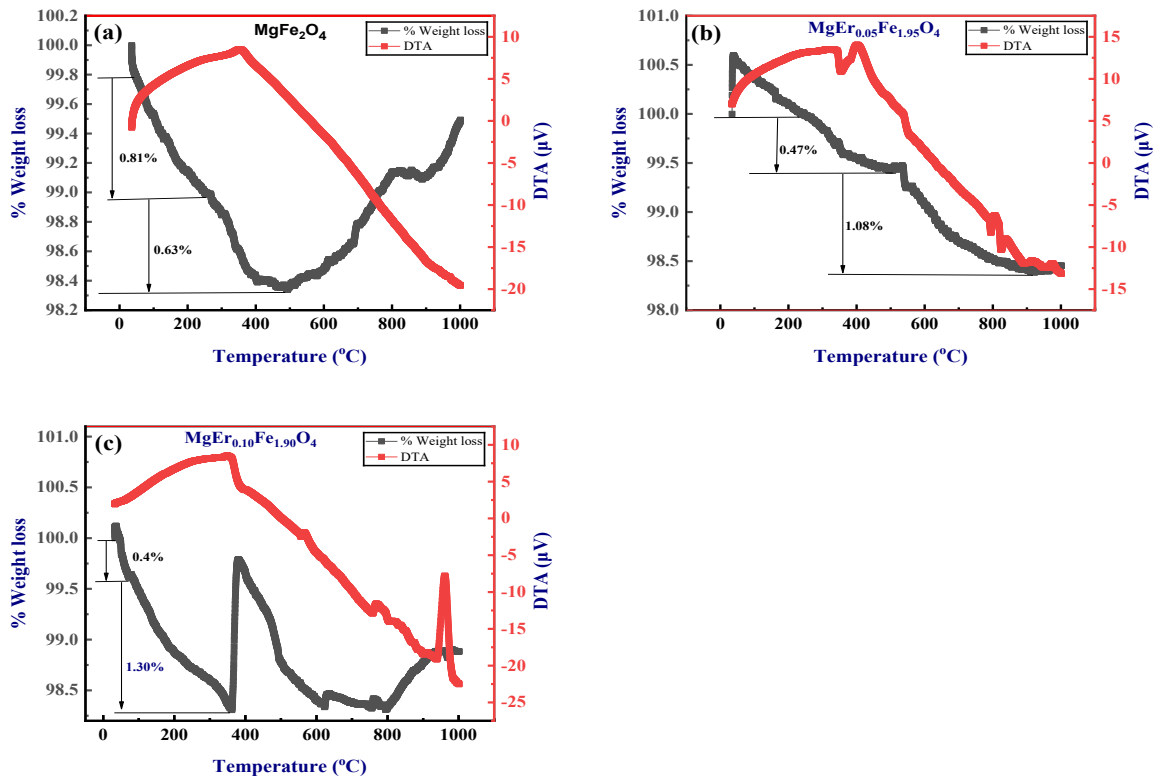

Fig.7 TG-DTA of $MgEr_xFe_{2-x}O_4$ (x = 0.00, 0.05 and 0.10) ferrites.

about 205 - 206 °C, which corresponds to the crystallization of the $MgFe_2O_4$spinel phase. This behavior is typical for pure ferrites, where crystallite ordering occurs at moderate temperatures when adsorbed moisture and leftover organics are removed [24, 25]. Together with a sharp increase in heat-flow intensity, the crystallization and melting temperatures rise to approximately 395 °C and 396 °C, respectively, at x = 0.05. As has been extensively documented in rare-earth-modified ferrites, such an increase in thermal transition temperatures suggests improved structural stiffness and stronger metal - oxygen bonding as a result of dopant incorporation [25]. Partial lattice relaxation and decreased phase stability at greater dopant content are indicated by the transitions shifting southward once again (~296 - 297 °C) for x = 0.10, along with decreased heat flow. Dopant-induced changes in defect density, oxygen vacancy formation, and cation redistribution are suggested by the progressive modulation of both the percentage weight loss and the DTA peak intensity across the compositions [25, 26]. These changes have a major impact on the thermal stability of spinel ferrites.

With x = 0.05 showing the highest crystallization and melting temperatures, indicating improved thermal stability, the TG - DTA curves demonstrate a significant dopant-dependent change in thermal transitions. In line with previous results on doped ferrites, the variations in heat-flow intensity reflect dopant-induced lattice deformation and changed cation - oxygen bonding.

4.Conclusions

All $MgEr_xFe_{2-x}O_4$ samples crystallise in a single-phase cubic spinel structure (Fd - 3m), according to Rietveld-refined XRD patterns. The UV - Vis absorption spectra of $MgEr_xFe_{2-x}O_4$ nanoparticles show a large absorption band in the 600 - 650 nm area, which is typical of spinel ferrites. Excellent agreement was found between the observed and estimated profiles without any secondary phases. Because of variations in cation distribution and lattice deformation, Er^{3+} substitution alters the absorption intensity. Reduced absorbance from longer annealing times suggests better crystallinity and fewer states linked to defects. These findings show that the optical characteristics of $MgEr_xFe_{2-x}O_4$ ferrites are efficiently tuned by both Er doping and thermal treatment. The optical band gap of $MgEr_xFe_{2-x}O_4$ ferrites can be effectively tuned by Er doping, which makes these materials attractive options for photocatalytic, sensor, and visible-light-driven optoelectronic applications. The DSC curves of $MgEr_xFe_{2-x}O_4$ exhibit a broad endothermic zone with no abrupt transitions up to 400 °C, showing strong thermal stability of the spinel phase, and an endothermic peak below ~100 °C due to moisture elimination. The heat-flow behavior is slightly altered by Er substitution, indicating better lattice stabilization without phase transformation. Progressive crystallization and lattice relaxation are indicated by expanded DSC curves, which display a slow increase in heat-flow without noticeable crystallization peaks. The crystallization slope is somewhat altered by Er substitution, indicating improved thermal stabilization and defect-controlled grain development devoid of phase change. With x = 0.05 showing the highest crystallization and melting temperatures, indicating improved thermal stability, the TG - DTA curves demonstrate a significant dopant-dependent change in thermal transitions.

References:

[1]. Goldman A. Modern Ferrite Technology. 2nd ed. Springer; 2006.

[2]. Valenzuela R. Magnetic Ceramics. Cambridge University Press; 1994.

[3]. Ranga R, Kumar K, Kumar A. (2023) Influence of rare-earth ion substitution on structural and magnetic properties of Mg-based spinel ferrites. Journal of Magnetism and Magnetic Materials. 588, 171496.

[4]. Pandey B, Srivastava RC, Joshi CS, Verma HK (2025). Effect of rare-earth ion doping on structural and magnetic behavior of ferrite nanoparticles. Physica B: Condensed Matter. 711, 417302.

[5]. Dojčinović MP, Vasiljević ZZ, Pavlović VP, et al. (2021) Structural and magnetic correlations in Mg-based spinel ferrites. Journal of Alloys and Compounds. 855, 157429.

[6]. Tangcharoen T. (2024) Structural stability and magnetic properties of $MgFe_2O_4$ spinel ferrite prepared at different calcination temperatures. Results in Materials. 23, 100596.

[7]. Islam S, Rahman ML, Moni MR, et al. (2023) Structural, optical and thermal properties of spinel ferrite nanoparticles synthesized via sol–gel route. Arabian Journal of Chemistry. 16, 105186.

[8]. Basfer NM, Al-Harbi N. (2023) Rare-earth-doped spinel ferrites: structural, optical and photocatalytic properties. Journal of King Saud University – Science.35, 102436.

[9]. Gabal MA, Al-Angari YM. (2020) Magnetic and electrical properties of rare-earth substituted magnesium ferrites. Ceramics International. 46, 20110–20118.

[10]. Slimani Y, Almessiere MA, Güngüneş H, et al. (2022) Rare-earth doped spinel ferrites for multifunctional applications. Journal of Materials Research and Technology. 18, 2030–2042.

[11]. A. T. Raghavender, D. Pajic, K. Zadro, T. Milekovic, P. V. Rao, K.M. Jadhav, D. Ravinder, (2007) Synthesis and magnetic properties of $NiFe_{2-x}Al_xO_4$ nanoparticles, Journal of Magnetism and Magnetic Materials 316 (1), 1-7

[12]. J. Adam, K. Vijaya Kumar, N. Hari Kumar, (2024), Er3+ ion-doped Mg-Zn nanoferrite: Properties and applications in dielectric, magnetic, structural, and optical domains affected by calcination temperature, Inorganic Chemistry Communications 167, 112698.

[13]. Young RA. The Rietveld method. IUCr Monographs on Crystallography. Oxford University Press; 1993.

[14]. Ranga R, Kumar K, Kumar A. (2023) Influence of Ce^{3+} ion doping on structural properties of spinel ferrite nanoparticles. Journal of Magnetism and Magnetic Materials. 588, 171496.

[15]. Dojčinović MP, Vasiljević ZZ, Pavlović VP, et al. (2021) Structure–property correlation in Mg-based spinel ferrites. Journal of Alloys and Compounds. 855, 157429.

[16]. Pandey B, Srivastava RC, Joshi CS, Verma HK.(2025) Effect of cerium ion doping on crystal structure of ferrite nanoparticles. Physica B: Condensed Matter. 711, 417302.

[17] Ranga R, Kumar K, Kumar A. (2023) Influence of Ce^{3+} ion doping on structural, magnetic, dielectric and optical properties of $Mg_{0.5}Ni_{0.5}Fe_{2-x}Ce_xO_4$ ferrite nanoparticles. Journal of Magnetism and Magnetic Materials. 588, 171496.

[18] Bouazizi ML, Hcini S, Khirouni K, et al. (2023) Annealing temperature effects on structural, magnetic and optoelectronic properties of spinel ferrites. Journal of Electronic Materials. 52, 2878–2893.

[19] Shashi Kumar Jakkaraju, Katrapally Vijaya Kumar, N. Hari Kumar, (2025) Influence of calcination temperature on gadolinium doped magnesium-zinc ferrite nanoparticles: Structural, optical, and photocatalytic properties for water splitting applications, Next Materials 8, 100705.

[20] TangcharoenT.(2024) Enhanced optical properties of $MgFe_2O_4$ spinel ferrite prepared under different calcination temperatures. *Results in Materials*. 23,100596.

[21] Dojčinović MP, Vasiljević ZZ, Pavlović VP, et al. (2021) Mixed Mg–Co spinel ferrites: Structure, magnetic and photocatalytic properties. *Journal of Alloys and Compounds*. 855, 157429.

[22] Basfer NM, Al-Harbi N. (2022) Structural and optical properties of Ce^{3+}-doped Co–Mg ferrite nanoparticles. *Journal of King Saud University – Science*. 35, 102436.

[23] Pandey B, Srivastava RC, Joshi CS, Verma HK. (2023) Effect of cerium ion doping on structural and electronic properties of ferrite nanoparticles. *Physica B: Condensed Matter*. 711, 417302.

[24] M.M. Rashad, S.S. Fouad, M.A. Azooz, (2017) Structural and thermal characterization of nanostructured MgFe2O4 powder prepared by sol-gel auto-combustion route, Journal of Thermal Analysis and Calorimetry, 128, 669–681.

[25] S. Ameen, M.A. Khan, (2018) Thermal analysis and phase transition behaviours of spinel ferrite nanoparticles Thermochimica Acta, 670, 50–58.

[26] L. Li, J. Wang, Y. Zhang (2019) Effect of dopants on thermal stability and structural properties of ferrites synthesized by co-precipitation Ceramics International, 45, 5427–5435.